# Optimal, Low-Thrust, Path-Constrained Transfers between Libration Point Orbits using Invariant Manifolds

J. R. Stuart,[*] M. T. Ozimek,[†] K. C. Howell[‡]

*Purdue University, West Lafayette, IN, 47907-2045, USA*

**Low-thrust transfers between libration point orbits can be applied in many potential mission scenarios, such as extended science missions or cargo transport. This investigation considers the inclusion of a variable specific impulse engine into a primer vector-based, fuel optimizing transfer strategy. A multiple shooting procedure with analytical gradients yields rapid solutions and offers an investigation into the trade space between flight time and consumption of fuel mass. Path and performance constraints can be included at node points along the thrust arc. Integration of invariant manifolds into the design strategy, for greater fuel savings, may also yield improved performance.**

## Nomenclature

| | |
|---|---|
| $\boldsymbol{x}$, $\boldsymbol{\chi}$ | State Variable Vectors |
| $t$ | Time |
| $\boldsymbol{r}$, $\boldsymbol{v}$ | Position and Velocity Vectors, Earth-moon Rotating Frame |
| $m$ | Spacecraft mass |
| $\boldsymbol{f_1}$ | Natural System Acceleration |
| $T$ | Thrust |
| $P$ | Engine Power |
| $\boldsymbol{u}$ | Thrust Direction Unit Vector |
| $d_1$, $d_2$ | Earth and moon Distances |
| $\mu$ | Mass Parameter |
| $I_{sp}$ | Specific Impulse |
| $\boldsymbol{\Phi}$, $\boldsymbol{\Psi}$ | State Transition Matrices |
| $\hat{\boldsymbol{v}}$ | Normalized Eigenvector |
| $\boldsymbol{A}$ | Gradient of Change in State with respect to State |
| $\delta$ | Manifold Scaling Value |
| $\tau$ | Periodic Orbit Time-like Parameter |
| $\alpha$ | Manifold Time-like Parameter |
| $TD$ | Thrust Duration |
| $J$ | Cost Function |
| $H$ | Problem Hamiltonian |
| $\boldsymbol{\lambda}$ | Co-states |
| $\boldsymbol{\psi}$ | Boundary Conditions |
| $S$ | Switching Function |

---

[*] Graduate Student, School of Aeronautics and Astronautics, Purdue University, Armstrong Hall of Engineering, 701 W. Stadium Ave, West Lafayette, Indiana 47907-2045; Student Member AIAA.

[†] Ph.D., School of Aeronautics and Astronautics, Purdue University, Armstrong Hall of Engineering, 701 W. Stadium Ave, West Lafayette, Indiana 47907-2045; Currently Senior Staff at Johns Hopkins University Applied Physics Laboratory, 11100 Johns Hopkins Road, Laurel, Maryland 20723-6099; Member AIAA.

[‡] Hsu Lo Professor of Aeronautical and Astronautical Engineering, School of Aeronautics and Astronautics, Purdue University, Armstrong Hall of Engineering, 701 W. Stadium Ave, West Lafayette, Indiana 47907-2045; Fellow AAS; Associate Fellow AIAA.

| | |
|---|---|
| $\boldsymbol{\chi}$ | Combined State and Co-State Vector |
| $\boldsymbol{a}$ | Time Rate of Change of $\boldsymbol{\chi}$ |
| $n$ | Number of Segments |
| $X$ | Full State Vector |
| $F$ | Constraint Vector |
| $DF$ | Gradient of Constraint Vector |
| $\kappa$ | Constraint Slack Variable |

## I. Introduction

Several future mission concepts might be enabled with efficient, low-thrust transfers between unstable libration point orbits. For example, the small transfer propellant requirements may allow a spacecraft to shift into several different science orbits over the course of a single mission. Also, for multiple satellite missions, one spacecraft may require a rendezvous with a spacecraft in a different orbit. These multiple spacecraft applications might be part of a baseline mission, but there is also the possibility for cargo transfer, that is, arriving at and departing from a fuel depot. Additional fuel savings are also possible by exploiting the unstable and stable invariant manifolds of the respective departure and arrival orbits. The use of low-thrust propulsion to achieve such transfers also introduces a wide array of potential solutions that span the trade space of propellant requirement and time-of-flight. Thus, one goal of this research is a trajectory computation strategy that yields many trajectories that solve the problem. With these solutions available, a trajectory designer can best select a solution that meets the fuel expenditure constraints given the time-of-flight considerations.

Given the nonlinear dynamics in the vicinity of libration point orbits, the design of optimal, low-thrust transfers typically involves the careful placement of coasting arcs to minimize the fuel. However, the timing, duration, and the determination of the number of coast arcs are all nontrivial issues in the design process. Operationally, shut-downs and restarts of the engine multiple times may also be infeasible. To mitigate these issues, a variable specific impulse engine is selected with the capability to vary the optimal thrust magnitude without turning the engine off.[1] Thus, the transfer only requires a single powered arc. Examples of VSI engines include the Variable Specific Impulse Magnetoplasma Rocket (VASIMR) currently under development by the Ad Astra Rocket Company[2] and the Electron and Ion Cyclotron Resonance (EICR) Plasma Propulsion Systems at Kyushu University in Japan.[3]

In general, the computation of locally fuel optimal trajectories is approached by posing an optimal control problem. The possible formulations to solve the problem include a low-dimension, but less robust indirect approach using optimal control theory[4–6] or a higher-dimension, but more robust direct approach.[7,8] (A detailed discussion of indirect and direct trajectory optimization methods is addressed in a survey by Betts.[9]) A third option is the implementation of a hybrid method that implements the optimal controls of the indirect approach, but neglects the sensitive transversality boundary conditions in favor of directly minimizing the cost. This concept is intended to increase the convergence radius, but preserve the low dimension of the problem, and has been previously explored by Kluever and Pierson[10] as well as Ozimek and Howell.[11] Due to the priority on rapidly computing many trajectories, the indirect and hybrid approaches are explored in detail. Relatively short times-of-flight (compared to long-duration spiral trajectories), the use of the hybrid approach, and continuation methods aid in achieving robust convergence.

In this paper, fuel optimal transfers between periodic orbits near the collinear libration points incorporating a variable specific impulse (VSI) engine are computed using Primer Vector Theory.[12] To address the difficulties of applying constraints using indirect optimization, the method of multiple shooting is combined with direct optimization techniques to apply constraints at specific node points along the transfer. Many candidate solutions are investigated, showing the trade-off between thrust duration, final mass, and different initial and final orbits. The optimal transfers also incorporate the option of coast arcs along the invariant manifolds associated with the periodic orbits. After the general optimization and multiple shooting processes are developed, a series of specific applications are investigated:

(i) transfer between orbits in the vicinity of the same collinear point;
(ii) transfer between orbits identified with different collinear points;
(iii) transfer with the inclusion of performance constraints.

The libration point orbits are a mix of northern and southern halos near both $L_1$ and $L_2$ as well as a vertical orbit near $L_1$.

## II. System Model

### A. Equations of Motion

The dynamic model is based on the Circular Restricted Three Body Problem (CR3BP) with the Earth as one primary and the moon as the second. The equations of motion are constructed within the context of a rotating reference frame where $\hat{x}$ is directed from the Earth to the moon, $\hat{z}$ is normal to the orbital plane of the primaries and in the same direction as their angular momentum, and $\hat{y}$ completes the right-handed set. The coordinate system is centered on the system barycenter. Also included in the dynamical model are the states and terms that arise from the thrusting of the Variable Specific Impulse (VSI) engine. The system is non-dimensionalized to aid numerical integration efficiency: computed results can then be converted to dimensional quantities by the proper use of the characteristic quantities and spacecraft parameter values. The gravitational acceleration terms are non-dimensionalized by the Earth-moon distance, the mass of the primaries, and the characteristic time, while the quantities in the thrust terms are non-dimensionalized by the Earth-moon distance, the initial spacecraft mass, and the characteristic time. The state of the spacecraft is defined as:

$$\boldsymbol{\chi} = \begin{Bmatrix} \boldsymbol{r} \\ \boldsymbol{v} \\ m \end{Bmatrix} \tag{1}$$

where $\boldsymbol{r}$ is the position vector from the barycenter, $\boldsymbol{v}$ is the velocity vector with respect to the barycenter as viewed by a rotating observer, and $m$ is the instantaneous mass of the spacecraft. The equations of motion are then:

$$\dot{\boldsymbol{\chi}} = \begin{Bmatrix} \dot{\boldsymbol{r}} \\ \dot{\boldsymbol{v}} \\ \dot{m} \end{Bmatrix} = \begin{Bmatrix} \boldsymbol{v} \\ \boldsymbol{f}_1(\boldsymbol{r},\boldsymbol{v}) + \frac{T}{m}\boldsymbol{u} \\ -\frac{T^2}{2P} \end{Bmatrix} \tag{2}$$

where $T$ is thrust magnitude, $P$ is engine power, $\boldsymbol{u}$ is a unit vector defining the thrust direction, and $\boldsymbol{f}_1$ represents the natural gravitational acceleration of the spacecraft. The scalar elements of $\boldsymbol{f}_1$ are derived in terms of the barycentered rotating frame:

$$\boldsymbol{f_1} = \begin{Bmatrix} 2\dot{y} + x - \frac{(1-\mu)(x+\mu)}{d_1^3} - \frac{\mu(x+\mu-1)}{d_2^3} \\ -2\dot{x} + y - \frac{(1-\mu)y}{d_1^3} - \frac{\mu y}{d_2^3} \\ -\frac{(1-\mu)z}{d_1^3} - \frac{\mu z}{d_2^3} \end{Bmatrix} \tag{3}$$

where $d_1$ and $d_2$ are the distances from the Earth and the moon respectively:

$$d_1 = \sqrt{(x+\mu)^2 + y^2 + z^2} \tag{4}$$

$$d_2 = \sqrt{(x+\mu-1)^2 + y^2 + z^2} \tag{5}$$

The mass parameter $\mu$ is defined as

$$\mu = \frac{M_m}{M_e + M_m} \tag{6}$$

where $M_e$ and $M_m$ are the masses of the Earth and the moon. The power $P$ is restricted to be a scalar value between zero and a maximum power level specified by the engine model, such that

$$0 \leq P \leq P_{\max} \tag{7}$$

The thrust $T$ of the engine is calculated via

$$T = \frac{2P}{I_{sp} g_0} \tag{8}$$

where $I_{sp}$ is the engine specific impulse and $g_0 = 9.81$ m/s$^2$, the gravitational acceleration at the surface of the Earth. Information on the system and spacecraft is available in Table 1.

**Table 1. System and spacecraft parameter values.**

| Quantity | Value | Units |
|---|---:|---|
| Earth mass ($M_e$) | $5.972\times10^{24}$ | kg |
| Lunar mass ($M_m$) | $7.346\times10^{22}$ | kg |
| Mass parameter ($\mu$) | 0.01215 | NA |
| Earth moon distance ($l^*$) | 384400 | km |
| Characteristic Time ($t^*$) | $3.752\times10^{5}$ | sec |
| Characteristic Time ($t_d^*$) | 4.342 | days |
| Initial spacecraft mass ($m_0$) | 500 | kg |
| Maximum spacecraft power ($P_{\max}$) | 2.0 | kW |

## B. Invariant Manifolds

In the uncontrolled CR3BP model, unstable collinear libration point orbits of period $\mathbb{P}$ possess a higher-dimensional surface of stable and unstable flow that can be exploited for the design of transfer trajectories. The numerical propagation of either of these originates by perturbing an initial state on the periodic orbit, $\boldsymbol{x}(t_i) = [\boldsymbol{r}(t_i)^T, \boldsymbol{v}(t_i)^T]^T$, in the direction of the local stable or unstable eigenvector associated with the monodromy matrix $\boldsymbol{\Phi}(t_i + \mathbb{P}, t_i)$ by some scale value, $\delta$. The state transition matrix (STM) is defined such that

$$\boldsymbol{\Phi}(t, t_i) = \frac{\partial \boldsymbol{x}(t)}{\partial \boldsymbol{x}(t_i)} \tag{9}$$

$$\dot{\boldsymbol{\Phi}}(t, t_i) = \frac{\partial \boldsymbol{f}}{\partial \boldsymbol{x}}\boldsymbol{\Phi}(t, t_i) = \mathbf{A}_6(t)\boldsymbol{\Phi}(t, t_i) \tag{10}$$

$$\boldsymbol{\Phi}(t_i, t_i) = \mathbf{I}_6 \tag{11}$$

Note that $\boldsymbol{f} = \left(\boldsymbol{v}^T, \boldsymbol{f}_1^T\right)^T$, and $\mathbf{I}_6$ corresponds to a $6 \times 6$ identity matrix. If the eigenvectors associated with the stable and unstable eigenvalues are defined as

$$\hat{\gamma}^s(t_i) = \begin{pmatrix} x_s & y_s & z_s & \dot{x}_s & \dot{y}_s & \dot{z}_s \end{pmatrix}^T \tag{12}$$

$$\hat{\gamma}^u(t_i) = \begin{pmatrix} x_u & y_u & z_u & \dot{x}_u & \dot{y}_u & \dot{z}_u \end{pmatrix}^T \tag{13}$$

respectively, then a normalization results in the definitions,

$$\begin{aligned} \hat{v}^s(t_i) &= \frac{\hat{\gamma}^s(t_i)}{\left|\hat{\gamma}^s(t_i)\right|} \\ \hat{v}^u(t_i) &= \frac{\hat{\gamma}^u(t_i)}{\left|\hat{\gamma}^u(t_i)\right|} \end{aligned} \tag{14}$$

Note that the eigenvectors, $\hat{\gamma}^s(t_i)$ and $\hat{\gamma}^s(t_i)$, are available from the monodromy matrix at the appropriate fixed point, $\boldsymbol{\Phi}(\mathbb{P} + t_i, t_i)$. The initial states, approximations to the unstable and stable manifold state vectors, are then computed as

$$\begin{aligned} \boldsymbol{x}_s(t_i) &= \boldsymbol{x}(t_i) \pm \delta \cdot \hat{v}^s \\ \boldsymbol{x}_u(t_i) &= \boldsymbol{x}(t_i) \pm \delta \cdot \hat{v}^u \end{aligned} \tag{15}$$

The alternating signs on the displacement from $\boldsymbol{x}(t_i)$ in Eq.(15) represent the fact that the trajectory may be perturbed from the eigenvector in either direction in the stable or unstable subspace. Propagating the states, $\boldsymbol{x}_s(t_i)$, in negative time from a set of fixed locations along the entire orbit results in globalization of the stable manifold. Repeating the process in the unstable subspace, i.e., propagating from the states, $\boldsymbol{x}_u(t_i)$, in positive time results in globalization of the unstable manifold. Globalization of the unstable manifolds for an Earth-moon $L_1$ halo orbit and the stable manifolds for an Earth-moon $L_2$ halo orbit appear in Fig. 1. The individual trajectories in Fig. 1 are merely illustrative paths along the manifold surface. For implementation in numerical search algorithms, any trajectory of interest, associated with either the stable or unstable manifold, is quickly computed by parameterizing the surface with two time-like parameters, $\tau$ and $\alpha$, consistent with Fig. 2. Here, $\tau$ indicates the departure location from the periodic orbit with respect to a reference point, and $\alpha$ reflects the propagation duration along the manifold. For this paper, the reference for $\tau$ is the northern $xz$-plane crossing for the northern halos and the vertical orbit and the southern $xz$-plane crossing for the southern halos.

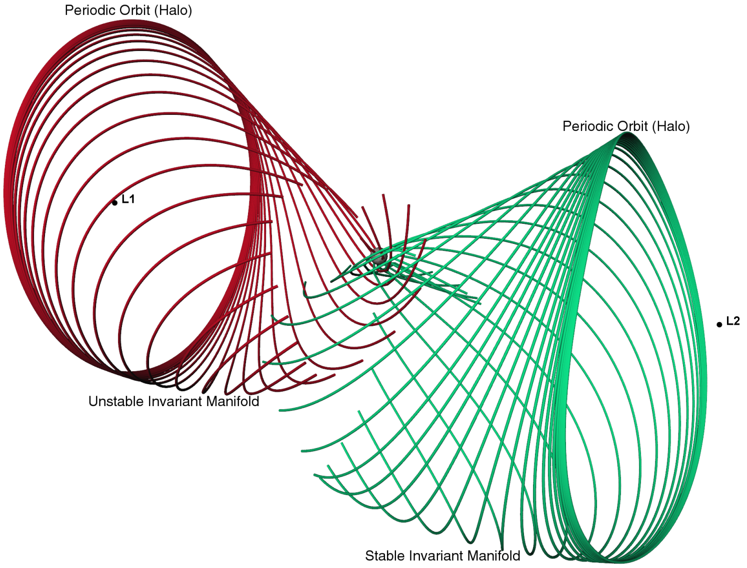

**Figure 1. Stable (green) and unstable (red) Earth-moon halo orbit manifold trajectories.**

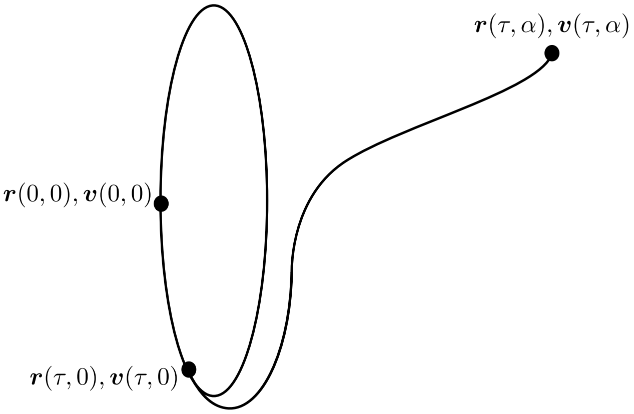

**Figure 2. Illustration of manifold parameters.**

## III. Trajectory Optimization

For unconstrained transfers, the calculus of variations can be used to indirectly solve the optimization problem in terms of a two-point boundary value problem (2PBVP). However, the thrust duration $TD$ must be specified since a VSI engine is employed: if no limit is placed on either the thrust duration or the minimum mass consumed, the optimization process drives $TD$ and $I_{sp}$ to infinity while consuming zero propellant mass. The goal is maximization of the spacecraft final mass for a specified thrust duration, so the performance index $J$ is defined

$$\max J = m_f \tag{16}$$

The performance index is modified by the boundary conditions and the Hamiltonian, so that Eq. (16) becomes the Bolza function

$$\max J' = m_f + \boldsymbol{\nu}_0^T \boldsymbol{\psi}_0 + \boldsymbol{\nu}_f^T \boldsymbol{\psi}_f + \int_{t_0}^{t_f} [H - \boldsymbol{\lambda}^T \dot{\boldsymbol{\chi}}] dt \tag{17}$$

where $H$ is the problem Hamiltonian, $\boldsymbol{\lambda}$ is a co-state vector, the $\boldsymbol{\psi}$ terms are boundary conditions, and the terms involving $\boldsymbol{\nu}$ are Lagrange multipliers for the boundary conditions. The co-state vector is

$$\boldsymbol{\lambda} = \begin{Bmatrix} \boldsymbol{\lambda_r} \\ \boldsymbol{\lambda_v} \\ \lambda_m \end{Bmatrix} \tag{18}$$

where $\boldsymbol{\lambda_r}$ and $\boldsymbol{\lambda_v}$ are vectors comprised of the position and velocity co-states, respectively, and $\lambda_m$ is the mass co-state. The initial and final boundary conditions are

$$\boldsymbol{\psi}_0 = \boldsymbol{x}_I - \boldsymbol{x}_I(\tau_0, \alpha_0) = \mathbf{0} \tag{19}$$

and

$$\boldsymbol{\psi}_f = \boldsymbol{x}_T - \boldsymbol{x}_T(\tau_f, \alpha_f) = \mathbf{0} \tag{20}$$

where the subscripts $I$ and $T$ indicate the initial and target states on the invariant manifolds or periodic orbits, respectively. If either one of the invariant manifolds is not used for a specific mission application, then the corresponding manifold parameter $\alpha$ can be set to zero and the boundary value problem can be simplified accordingly. Equation (19) is satisfied by defining $\boldsymbol{x}_I$ as the state on the unstable manifold as defined by $\tau_0$ and $\alpha_0$. If the mission objective is the transfer from orbit to orbit without using the unstable invariant manifold then, recall from Fig. 2, that $\boldsymbol{x}_0$ is the position and velocity on the initial periodic orbit at the point represented by the parameter $\tau_0$.

Calculus of variations is employed to define several properties of the 2PBVP and acquire the derivatives of the co-states. The problem Hamiltonian is

$$H = \boldsymbol{\lambda}^T \dot{\boldsymbol{\chi}} = \boldsymbol{\lambda_r}^T \boldsymbol{v} + \boldsymbol{\lambda_v}^T \left[ \boldsymbol{f}_1(\boldsymbol{r}, \boldsymbol{v}) + \frac{T}{m} \boldsymbol{u} \right] - \lambda_m \frac{T^2}{2P} \tag{21}$$

where the value of $H$ is constant over the entire trajectory. The optimal controls are obtained by maximizing the Hamiltonian with respect to the controls $T$, $P$, and $\boldsymbol{u}$ so that

$$P = P_{\max} \tag{22}$$

$$T = \frac{\lambda_v P_{\max}}{\lambda_m m} \tag{23}$$

$$\boldsymbol{u} = \frac{\boldsymbol{\lambda_v}}{\lambda_{\boldsymbol{v}}} \tag{24}$$

where $\lambda_{\boldsymbol{v}}=||\boldsymbol{\lambda_v}||$. From these controls, the Hamiltonian, Eq. (21), is reformulated to

$$H = \boldsymbol{\lambda_r}^T \boldsymbol{v} + \boldsymbol{\lambda_v}^T \boldsymbol{f}_1 + S \cdot T \tag{25}$$

where $S$ is the switching function

$$S = \frac{\lambda_{\boldsymbol{v}}}{m} - \frac{\lambda_m T}{2P_{\max}} \tag{26}$$

Applying the Euler-Lagrange conditions for optimality to the modified performance index in Eq. (17), with the reformulated Hamiltonian, Eq. (25), yields the following equations of motion for the co-states:

$$\dot{\boldsymbol{\lambda}} = -\left(\frac{\partial H}{\partial \boldsymbol{\chi}}\right)^T = \begin{Bmatrix} -\boldsymbol{\lambda_v}^T \left(\frac{\partial \boldsymbol{f}_1}{\partial \boldsymbol{r}}\right) \\ -\boldsymbol{\lambda_r}^T - \boldsymbol{\lambda_v}^T \left(\frac{\partial \boldsymbol{f}_1}{\partial \boldsymbol{v}}\right) \\ \lambda_{\boldsymbol{v}} \frac{T}{m^2} \end{Bmatrix} \tag{27}$$

where the initial state for $\lambda_m$ is set to unity to reduce the number of variables to be determined.

All that remains in defining the 2PBVP is construction of the transversality conditions to ensure local optimality. The first differentials of the Bolza function, Eq. (17), with respect to the independent time-like parameters $\tau$ and $\alpha$ provide these conditions:

$$\boldsymbol{\lambda}_{\boldsymbol{rv}_0}^T \frac{\partial \boldsymbol{x}_I(\tau_0, \alpha_0)}{\partial \tau_0} = 0 \tag{28}$$

$$\boldsymbol{\lambda}_{\boldsymbol{rv}_0}^T \frac{\partial \boldsymbol{x}_I(\tau_0, \alpha_0)}{\partial \alpha_0} = 0 \tag{29}$$

$$\boldsymbol{\lambda}_{\boldsymbol{rv}_f}^T \frac{\partial \boldsymbol{x}_T(\tau_f, \alpha_f)}{\partial \alpha_f} = 0 \tag{30}$$

$$\boldsymbol{\lambda}_{\boldsymbol{rv}_f}^T \frac{\partial \boldsymbol{x}_T(\tau_f, \alpha_f)}{\partial \tau_f} = 0 \tag{31}$$

If a particular transfer design bypasses the use of one or both manifolds, then either or both of Eqs. (29) and (30) are omitted from the boundary value problem. The differential of the manifold trajectory with respect to the parameter $\alpha$ is simply

$$\frac{\partial \boldsymbol{x}}{\partial \alpha} = \begin{Bmatrix} \boldsymbol{v} \\ \boldsymbol{f}_1 \end{Bmatrix} \frac{\partial t}{\partial \alpha} \tag{32}$$

For the differential of the manifold trajectory with respect to the orbit parameter $\tau$, a more complex expression is developed that incorporates the insertion onto the manifold as well as the STM along the manifold. From Senent,[6] this expression is

$$\frac{\partial \boldsymbol{x}}{\partial \tau} = \boldsymbol{\Phi}(\alpha, 0)\boldsymbol{\Upsilon}(\tau) = \boldsymbol{\Phi}(\alpha, 0)\Big[\boldsymbol{f}(\boldsymbol{x}(\tau, 0)) + d_M[\mathbf{I}_6 - \hat{\boldsymbol{v}}(\tau)\hat{\boldsymbol{v}}(\tau)^T]\mathbf{A}_6(\boldsymbol{x}(\tau, 0))\hat{\boldsymbol{v}}(\tau)\Big]\frac{dt}{d\tau} \tag{33}$$

The fixed-time transfer between periodic orbits, with or without the use of invariant manifolds, is now formulated as a 2PBVP with a design variable vector consisting of the initial and target orbit parameters $\tau$ and $\alpha$ and the initial values of the co-state vectors $\boldsymbol{\lambda}_{\boldsymbol{r}}$ and $\boldsymbol{\lambda}_{\boldsymbol{v}}$. The optimization problem is solved using any boundary value problem or equation solver. This analysis employs the *fsolve* function in **MATLAB**.

Sometimes, the 2PBVP arising from the optimal control approach possesses transversality conditions that are particularly sensitive to satisfy or cumbersome to derive. An alternative strategy that requires minimal reformulation is to pose the problem as a direct optimization problem while maintaining the optimal controls (Eqs. (22)-(24)) from the indirect approach. This alternative formulation has previously been described as a hybrid method.[10] In developing a hybrid scheme, Eqs. (28)-(33) from the indirect formulation are ignored. Then, a cost function for the under-constrained problem is directly minimized with nonlinear programming (NLP) software. For this investigation, the sparse NLP software SNOPT is employed when the direct formulation is employed.[13] The hybrid direct approach is particularly useful for path-constrained optimization, where any general path constraints are added to the problem without updating the derivation of 2BVP transversality conditions.

## IV. Multiple Shooting Algorithm

Multiple shooting is the process of decomposing a trajectory into a series of segments. Each segment is defined by an initial patch point and constructed via propagation of the equations of motion. A multiple shooting algorithm reduces the effect of local sensitivities in calculating solutions, increases the accuracy of a solution, and allows for the relatively easy placement of constraints along a trajectory. This analysis primarily uses multiple shooting to apply constraints and to implement a continuation scheme where solutions for varying thrust durations are calculated given a known solution to the 2PBVP. To begin, define the combined state and co-state vector:

$$\boldsymbol{\xi} = \begin{Bmatrix} \boldsymbol{\chi} \\ \boldsymbol{\lambda} \end{Bmatrix} \tag{34}$$

with the associated associated vector derivative

$$\boldsymbol{a} = \dot{\boldsymbol{\xi}} = \begin{Bmatrix} \dot{\boldsymbol{\chi}} \\ \dot{\boldsymbol{\lambda}} \end{Bmatrix} \tag{35}$$

For an unconstrained transfer using multiple shooting with $n$ segments, the state vector is defined:

$$\boldsymbol{X} = \left\{ \begin{matrix} \tau_0 \\ \alpha_0 \\ \boldsymbol{\lambda}_1 \\ TD_1 \\ \boldsymbol{\xi}_2 \\ TD_2 \\ \vdots \\ \boldsymbol{\xi}_n \\ TD_n \\ \alpha_f \\ \tau_f \end{matrix} \right\} \tag{36}$$

where $\boldsymbol{\xi}_i$ is the combined state and co-state at the $i$-th patch point and $TD_i$ is the duration along the $i$-th segment. Segment duration is retained as a variable for greater flexibility when calculating solutions, though the consequence is a set of variables than is larger than strictly necessary for determining a solution. Note that, since the initial value of $\lambda_m$ is defined to be unity, $\boldsymbol{\lambda}_1$ is a 6-vector composed of only the initial position and velocity co-states associated with the thrust arc. The constraint vector is then expanded to include continuity constraints on the segments to ensure a smooth path:

$$\boldsymbol{F}(\boldsymbol{X}) = \left\{ \begin{matrix} \boldsymbol{\xi}_2^t(\tau_0, \alpha_0, \boldsymbol{\lambda}_1) - \boldsymbol{\xi}_2 \\ \boldsymbol{\xi}_3^t(\boldsymbol{\xi}_2) - \boldsymbol{\xi}_3 \\ \vdots \\ \boldsymbol{x}_T^t(\boldsymbol{\xi}_n) - \boldsymbol{x}_T(\tau_f, \alpha_f) \\ \boldsymbol{\lambda}_{\boldsymbol{rv}_1}^T \frac{\partial \boldsymbol{x}_I(\tau_0, \alpha_0)}{\partial \tau_0} \\ \boldsymbol{\lambda}_{\boldsymbol{rv}_1}^T \frac{\partial \boldsymbol{x}_I(\tau_0, \alpha_0)}{\partial \alpha_0} \\ \boldsymbol{\lambda}_{\boldsymbol{rv}_f}^T \frac{\partial \boldsymbol{x}_T(\tau_f, \alpha_f)}{\partial \alpha_f} \\ \boldsymbol{\lambda}_{\boldsymbol{rv}_f}^T \frac{\partial \boldsymbol{x}_T(\tau_f, \alpha_f)}{\partial \tau_f} \\ \sum_{i=1}^n TD_i - TD \end{matrix} \right\} = \boldsymbol{0} \tag{37}$$

where the superscript $t$ indicates states that are reached after propagation from a node for the associated segment duration. The final constraint in the vector $\boldsymbol{F}$ involves thrust durations and ensures that the overall transfer includes thrust durations that sum to the total specified value $TD$. The multiple shooting problem is solved by a boundary value problem solver or equation solver using either numerical or analytical gradients.

To construct the analytical gradients, however, a new state transition matrix encompassing the new co-states is developed. As before, the STM satisfies the following conditions

$$\dot{\boldsymbol{\Psi}}(t, t_0) = \frac{\partial \boldsymbol{a}}{\partial \boldsymbol{\xi}} \boldsymbol{\Psi}(t, t_0) = \mathbf{A}_{14}(t) \boldsymbol{\Psi}(t, t_0) \tag{38}$$

$$\boldsymbol{\Psi}(t_0, t_0) = \mathbf{I}_{14} \tag{39}$$

where, now, $\mathbf{A}_{14}(t)$ is the $14 \times 14$ variational matrix derived from Eqs. (2) and (27), given the states, Eq. (1) and co-states, Eq. (18). The expression for $\mathbf{A}_{14}(t)$ appears in the Appendix. Now, in representing the following form, the gradient of the constraint function, Eq. (37), with respect to the state vector, Eq. (36),

$$D\boldsymbol{F}(\boldsymbol{X}) =$$

$$\begin{bmatrix}
\boldsymbol{\Psi}_{1,\boldsymbol{rv}}\frac{\partial \boldsymbol{x}_I}{\partial \tau_0} & \boldsymbol{\Psi}_{1,\boldsymbol{rv}}\frac{\partial \boldsymbol{x}_I}{\partial \alpha_0} & \boldsymbol{\Psi}_{1,\lambda} & \boldsymbol{a}_1 & -\mathbf{I}_{14} & \mathbf{0} & \cdots & & \mathbf{0} \\
\mathbf{0} & \mathbf{0} & \mathbf{0} & \mathbf{0} & \boldsymbol{\Psi}_2 & \boldsymbol{a}_2 & -\mathbf{I}_{14} & \cdots & \mathbf{0} \\
\vdots & & & & & & & \ddots & \\
\mathbf{0} & \cdots & & \cdots & \mathbf{0} & -\mathbf{I}_{14} & \mathbf{0} & \mathbf{0} & \mathbf{0} \\
\mathbf{0} & \cdots & & \cdots & \mathbf{0} & \boldsymbol{\Psi}_{\boldsymbol{rv},n} & \boldsymbol{a}_n & -\frac{\partial \boldsymbol{x}_T}{\partial \alpha_f} & -\frac{\partial \boldsymbol{x}_T}{\partial \tau_f} \\
\boldsymbol{\lambda}^T_{\boldsymbol{rv}_1}\frac{\partial^2 \boldsymbol{x}_I}{\partial \tau_0^2} & \boldsymbol{\lambda}^T_{\boldsymbol{rv}_1}\frac{\partial^2 \boldsymbol{x}_I}{\partial \tau_0 \partial \alpha_0} & \left(\frac{\partial \boldsymbol{x}_I}{\partial \tau_0}\right)^T & \mathbf{0} & \cdots & & & & \mathbf{0} \\
\boldsymbol{\lambda}^T_{\boldsymbol{rv}_1}\frac{\partial^2 \boldsymbol{x}_I}{\partial \tau_0 \alpha_0} & \boldsymbol{\lambda}^T_{\boldsymbol{rv}_1}\frac{\partial^2 \boldsymbol{x}_I}{\partial \alpha_0^2} & \left(\frac{\partial \boldsymbol{x}_I}{\partial \alpha_0}\right)^T & \mathbf{0} & \cdots & & & & \mathbf{0} \\
\mathbf{0} & \cdots & & \cdots & \mathbf{0} & \left(\frac{\partial \boldsymbol{x}_T}{\partial \alpha_f}\right)^T \boldsymbol{\Psi}_{\boldsymbol{\lambda},n} & \boldsymbol{a}^T_{\boldsymbol{\lambda},n}\frac{\partial \boldsymbol{x}_T}{\partial \alpha_f} & \boldsymbol{\lambda}^T_{\boldsymbol{rv},f}\frac{\partial^2 \boldsymbol{x}_T}{\partial \alpha_f^2} & \boldsymbol{\lambda}^T_{\boldsymbol{rv},f}\frac{\partial^2 \boldsymbol{x}_T}{\partial \tau_f \partial \alpha_f} \\
\mathbf{0} & \cdots & & \cdots & \mathbf{0} & \left(\frac{\partial \boldsymbol{x}_T}{\partial \tau_f}\right)^T \boldsymbol{\Psi}_{\boldsymbol{\lambda},n} & \boldsymbol{a}^T_{\boldsymbol{\lambda},n}\frac{\partial \boldsymbol{x}_T}{\partial \tau_f} & \boldsymbol{\lambda}^T_{\boldsymbol{rv},f}\frac{\partial^2 \boldsymbol{x}_T}{\partial \tau_f \partial \alpha_f} & \boldsymbol{\lambda}^T_{\boldsymbol{rv},f}\frac{\partial^2 \boldsymbol{x}_T}{\partial \tau_f^2} \\
\mathbf{0} & \mathbf{0} & \mathbf{0} & 1 & \mathbf{0} & \cdots & 1 & \mathbf{0} & \mathbf{0}
\end{bmatrix} \tag{40}$$

where the variation in state $\boldsymbol{a}$ is evaluated at the end of each segment and the order of the subscripts on the $\boldsymbol{\Psi}$ state transition matrix indicates whether columns or rows are extracted. In the subscripts, a number preceding the variables indicates that columns are used, while a variable preceding a number reflects the fact that rows are employed (e.g., $\boldsymbol{\Psi}_{1,\boldsymbol{rv}}$ implies that the columns corresponding to the position and velocity states from the STM corresponding to the first segment are to be extracted).

Analytical expressions for the second partials of the initial and target states $\boldsymbol{x}_I$ and $\boldsymbol{x}_T$ are available in all cases. The partials with respect to the $\alpha$ parameters are all in the form:

$$\frac{\partial^2 \boldsymbol{x}(\tau,\alpha)}{\partial \alpha^2} = \mathbf{A}_{14}(\alpha)\begin{Bmatrix} \boldsymbol{v} \\ \boldsymbol{f}_1 \end{Bmatrix} \tag{41}$$

while, for the second partials with respect to both $\alpha$ and $\tau$, the expression is:

$$\frac{\partial^2 \boldsymbol{x}(\tau,\alpha)}{\partial \tau \partial \alpha} = \dot{\boldsymbol{\Phi}}(\alpha,0)\boldsymbol{\Upsilon}(\tau) \tag{42}$$

There does exist an analytical expression for $\frac{\partial^2 \boldsymbol{x}}{\partial \tau^2}$ but it is cumbersome and requires the second order mapping of initial to final states $\frac{\partial \boldsymbol{\Phi}(t,t_i)}{\partial \boldsymbol{x}(t_i)}$. Unfortunately, this process requires the integration of an *additional* 216 equations of motion. Thus, it is simply more computationally efficient to compute a numerical gradient for $\frac{\partial^2 \boldsymbol{x}}{\partial \tau^2}$. A brief note on implementation: for a large number of segments $n$, the sparse nature of the gradient matrix can be used to aid in computational efficiency.

## V. Mission Applications

### A. Orbit Transfer Families

The focus of the first application is the direct transfer from one northern $L_1$ halo orbit to another. Because the orbits are in the vicinity of the same collinear point, using the invariant manifolds offers little advantage if the transfer times are relatively short. Therefore, the terms $\alpha_0$ and $\alpha_f$ and their transversality conditions are omitted. The spacecraft transfers from the initial inner halo of lower $z$-amplitude to the final outer halo of higher $z$-amplitude, where $z$-amplitude is evaluated at the northern crossing of the $xz$-plane. Characteristics of the two orbits are summarized in Table 2.

Note that because the transversality conditions only assure local optimality, multiple solutions to the 2PBVP are available. Two families of locally optimal transfers appear in Fig. 3 and these are continued from an initial solution for a 2.4-day transfer. Family 1 originates in the lower right (positive $y$, negative $z$) of the initial (blue) halo, while Family 2 emanates from the lower left (negative $y$ and $z$) in the initial halo.

**Table 2. Halo orbit characteristics.**

| | **Initial Orbit** | **Final Orbit** | |
|---|---|---|---|
| Type | Northern Halo | Northern Halo | |
| $z$-amplitude | 17298 | 36518 | km |
| Period ($\mathbb{P}$) | 11.967 | 12.090 | days |
| Jacobi Constant | 3.1577 | 3.1091 | |

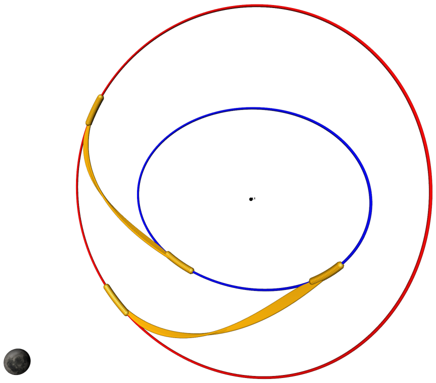

**Figure 3. Two families of locally optimal transfers.**

Notice that these transfers possess initial and final states that are relatively close within the family. The final mass of the spacecraft as a function of the transfer time is plotted in Fig. 4. For the shortest thrust duration, the transfer from Family 1 consumes about 5 more kg of mass than the transfer from Family 2; for longer times of flight, the difference in propellant consumption is less dramatic, but Family 1 always uses more mass to achieve a transfer of the same duration. Note that *all* transfer families included in this analysis demonstrate a similar asymptotic behavior when plotted against thrust duration, regardless of orbit type or the use of manifolds.

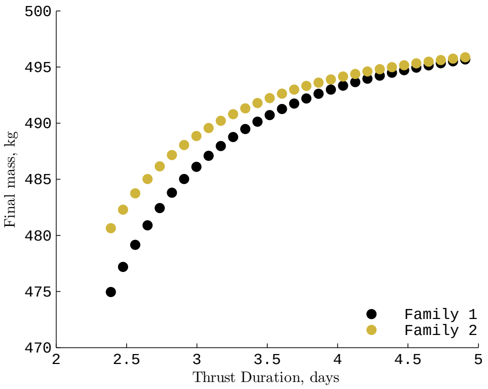

**Figure 4. Final mass of transfer families.**

Since Family 2 produces better performance for a given thrust duration, it will be used to investigate the transfer behavior for increasingly long times of flight. The transfer family, determined for thrust durations from 2.4 to 21.5 days appears in Fig. 5. Specific transfers corresponding to 2.4, 11.9, and 21.5 days of thrust are highlighted. An interesting feature of this transfer family is that all the end states are confined to the upper left (negative $y$, positive $z$) of the target halo. This region is not sharply defined in terms of the $xy$- and $xz$-planes, but is instead some distance from these two planes.

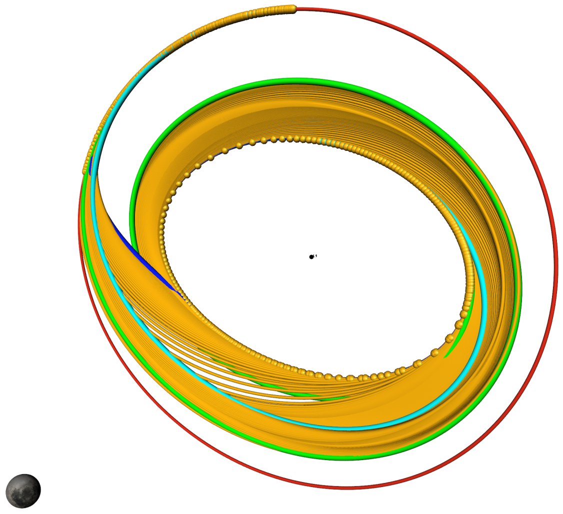

**Figure 5. Optimal transfers of thrust duration from 2.4 to 21.5 days.**

The transfers highlighted in Fig. 5 are isolated in Fig. 6, along with their respective $I_{sp}$ time histories. Note that, while the short duration transfer forms a more-or-less direct curve from the initial orbit to the target orbit, the two longer trajectory arcs complete one or (nearly) two revolutions before arrival. Also, the $I_{sp}$ profiles change drastically with increasing thrust duration, from one peak and no local minima to multiple local maxima and minima. Indeed, these $I_{sp}$ profiles begin to approximate thrust-coast-thrust architectures or a mixture of relatively low- and high-thrust arcs with coast arcs. For further investigation, the plots in Fig. 7 demonstrate the evolving nature of the maximum, average, and minimum $I_{sp}$, the target orbit parameter $\tau_f$, and the initial orbit parameter $\tau_0$ with respect to thrust duration. The change in $\tau_0$ is multiplied by a factor of 10 to better demonstrate its behavior. The "kinks" in the minimum and maximum $I_{sp}$ values coincide with the decrease in $\tau_f$ and rapid change in $\tau_0$, almost as if these two parameters act to "reset" the exponential growth in maximum $I_{sp}$ and the logarithmic growth in minimum $I_{sp}$. As a

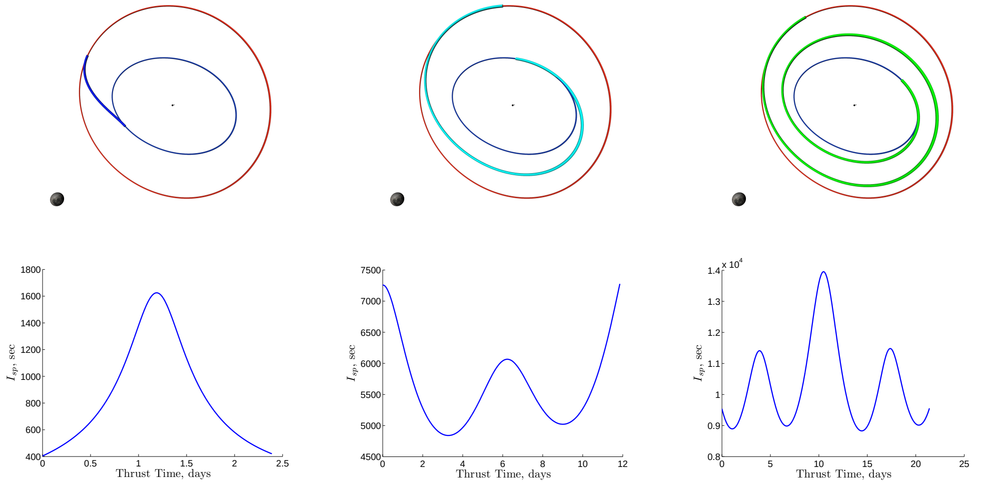

Thrust duration: 2.4 days Thrust duration: 11.9 days Thrust duration: 21.5 days

**Figure 6. Specific orbit transfers and their $I_{sp}$ profiles.**

consequence, the average $I_{sp}$ value increases nearly linearly.

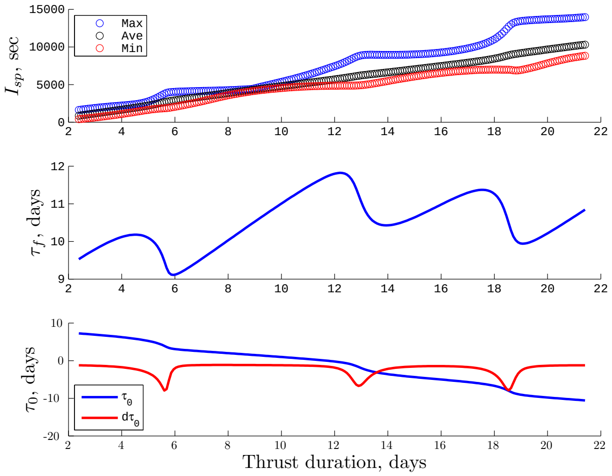

**Figure 7. Evolution of $I_{sp}$ and orbit parameters with respect to thrust duration.**

## B. Manifold Transfer Families

The second application under investigation involves transfers between libration point orbits that incorporate invariant manifolds. Two specific cases are investigated: transferring from an $L_1$ halo orbit to an $L_2$ halo orbit and transferring from an $L_1$ vertical orbit to an $L_2$ halo orbit.

### 1. *Example 1*

For the halo-to-halo transfer, the initial halo is an orbit from the northern family and the target halo is either a northern or southern halo with a Jacobi constant matched to the initial halo. Thus, the net effect of the VSI engine is to change the orbit but not the energy level. The information defining the departure and arrival halo orbits is summarized in Table 3.

**Table 3. $L_1$ and $L_2$ halo orbit characteristics.**

| | **Initial $L_1$ Orbit** | **Target $L_2$ Orbits** | | |
|---|---|---|---|---|
| Type | Northern Halo | Northern Halo | Southern Halo | |
| Z-amplitude | 34596 | 36997 | -36997 | km |
| Period ($\mathbb{P}$) | 12.080 | 14.480 | 14.480 | days |
| Jacobi Constant | 3.1149 | 3.1149 | 3.1149 | |

One possible set of transfers from the northern $L_1$ halo to both the northern and southern $L_2$ halos appears in Figure 8. The red arcs are coasts along the unstable manifold, green reflects coasts along the stable manifold, and gold represents the thrust arcs. These two families are composed of transfers with thrust durations from approximately 0.65 to 13 days. The arrivals on the northern halo stable manifold are relatively spread out and it is apparent that the thrust arcs radically change the spacecraft motion while transferring between the two manifolds. On the other hand, the transfers to the southern halo appear consistent with the natural dynamics in the CR3BP, that is, thrust arcs closely following the paths of the invariant manifolds. As is apparent in Fig. 9, for northern-to-southern transfers of increasing thrust duration there is not a drastic increase in overall transfer time nor is there a significant difference in the general flight path.

As previously mentioned, the plots of thrust duration versus final mass are very similar in profile for all the transfers. However, with the inclusion of the coast times along the invariant manifolds, the overall transfer time becomes an interesting new variable to compare relative to final mass: this relationship is plotted in

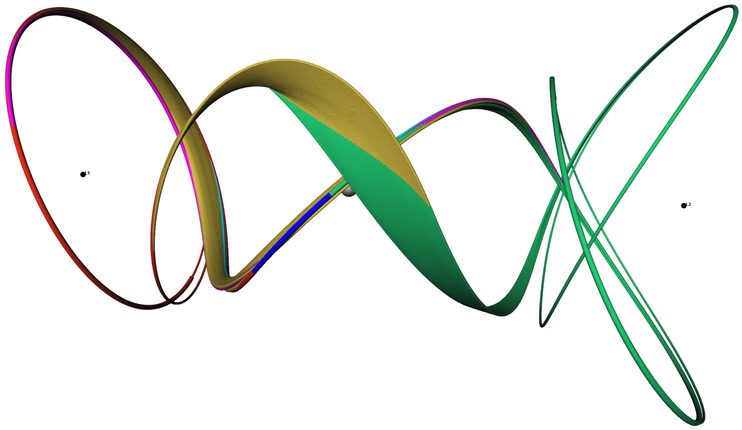

**Figure 8. Optimal transfers from a northern $L_1$ halo to both northern and southern halos using invariant manifolds.**

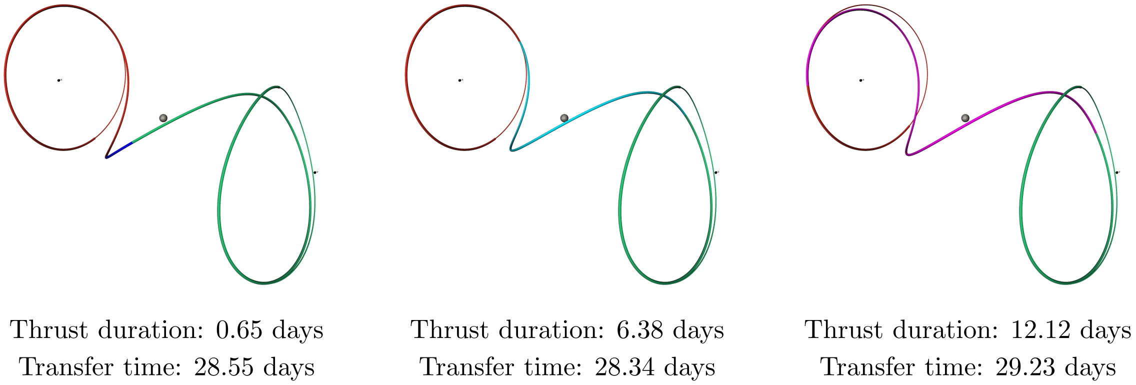
Thrust duration: 0.65 days
Transfer time: 28.55 days
Thrust duration: 6.38 days
Transfer time: 28.34 days
Thrust duration: 12.12 days
Transfer time: 29.23 days

**Figure 9. Specific northern $L_1$ halo to southern $L_2$ halo transfers.**

Fig. 10 for both target orbits. Clearly, the transfers to the southern $L_2$ halo are more fuel efficient and of shorter overall duration than the transfers to the northern halo. In this example, the transfer that "switches the hemisphere" between the initial and target halos (i.e., a north-to-south transfer) is more efficient in exploiting natural system dynamics and, thus, conserves both mass and flight time. Additional analysis is warranted. Furthermore, it is apparent that, for both families, there are some instances where a longer thrust duration, in addition to using less mass, also leads to a shorter overall transfer time.

### *2. Example 2*

In the second case that incorporates invariant manifolds, the spacecraft transfers from an $L_1$ vertical orbit to the two target $L_2$ halos from the first example. The vertical orbit possesses a different Jacobi constant than the target halos, so use of the VSI engine also changes the energy level. The characteristics describing the vertical orbit as well as the two halo orbits are summarized in Table 4.

Two families of transfers from the vertical orbit to the halos appear in Fig. 11; the total thrust duration ranges from 0.65 to 4.7 days. Immediately noticeable is the symmetry associated with the two families: the families appear nearly mirrored across the $xy$-plane. This symmetry implies that the two families should also possess many other similar characteristics, which is indeed true. Among other similarities, the families are represented by identical curves for final mass versus thrust duration and transfer time. From a design perspective, this symmetry can be exploited by focusing on transfers only to *one* of the target halos and then translating the results to the other halo. As is inferred from Fig. 12, this translation is a relatively simple procedure: switch the signs on the $z$ position and velocity co-states and shift the initial orbit parameter by

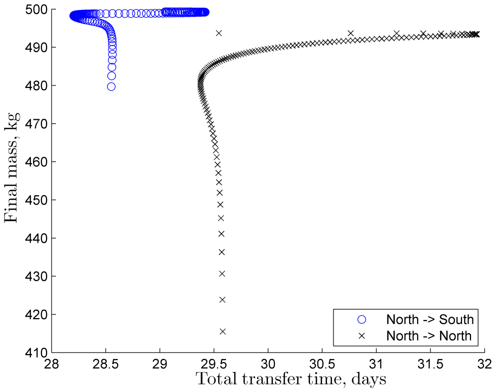

**Figure 10. Behavior of final mass with respect to the total transfer time between $L_1$ and $L_2$ halos.**

**Table 4. Vertical and halo $L_1$ and $L_2$ orbit characteristics.**

| | **Initial $L_1$ Orbit** | **Target $L_2$ Orbits** | | |
|---|---|---|---|---|
| Type | Vertical | Northern Halo | Southern Halo | |
| Z-amplitude | 97362 | 36997 | -36997 | km |
| Period ($\mathbb{P}$) | 18.238 | 14.480 | 14.480 | days |
| Jacobi Constant | 2.9793 | 3.1149 | 3.1149 | |

one-half period.

## C. Constrained Trajectories

One of the chief advantages of multiple shooting is the ability to add constraints to the patch points. As an example, an inequality constraint is placed on allowable $I_{sp}$ to simulate limitations on engine performance:

$$I_{sp,\text{limit,lower}} \leq I_{sp} \leq I_{sp,\text{limit,upper}} \tag{43}$$

The first step is the modification of the constraint function (37) to include the new constraints on the patch points:

$$\boldsymbol{F}(\boldsymbol{X}) = \begin{Bmatrix} I_{sp,1} - I_{sp,\text{limit}} \pm \kappa_1^2 \\ \boldsymbol{\xi}_2^t(\tau_0, \alpha_0, \boldsymbol{\lambda}_1) - \boldsymbol{\xi}_2 \\ I_{sp,2} - I_{sp,\text{limit}} \pm \kappa_2^2 \\ \boldsymbol{\xi}_3^t(\boldsymbol{\xi}_2) - \boldsymbol{\xi}_3 \\ \vdots \\ \boldsymbol{x}_T^t(\boldsymbol{\xi}_n) - \boldsymbol{x}_T(\tau_0, \alpha_0) \\ I_{sp,T} - I_{sp,\text{limit}} \pm \kappa_T^2 \end{Bmatrix} = \boldsymbol{0} \tag{44}$$

where the new variables $\kappa_i$ are slack variables with the appropriate sign to enforce the inequality constraint. An $I_{sp}$ constraint is applied to each of the patch points, with the exception of the final constraint with the subscript $T$: this constraint is applied at the final state along the thrust arc. This formulation assumes that only one of the $I_{sp}$ limits is being applied at each patch point, requiring *a priori* knowledge of the limit that each patch point is most likely to violate. However, both constraints are easily applied to each patch point, if so desired. Also note that the transversality conditions are removed as SNOPT is used to directly optimize $m_f$. The time-of-flight constraint is also removed because the trajectory segments are now defined with a fixed duration. The fixed segment duration ensures that the patch points do not simply move to a

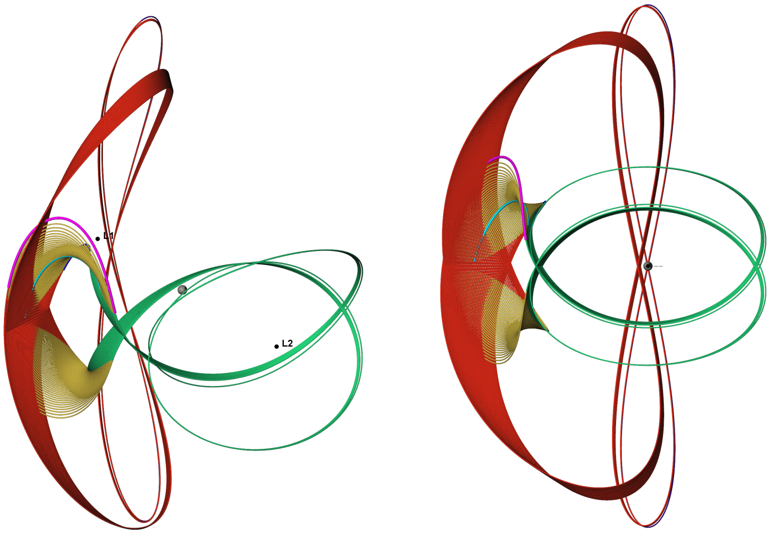

Off axis view     View down the $x$-axis

**Figure 11. Two views of transfers from $L_1$ vertical to $L_2$ northern and southern halos.**

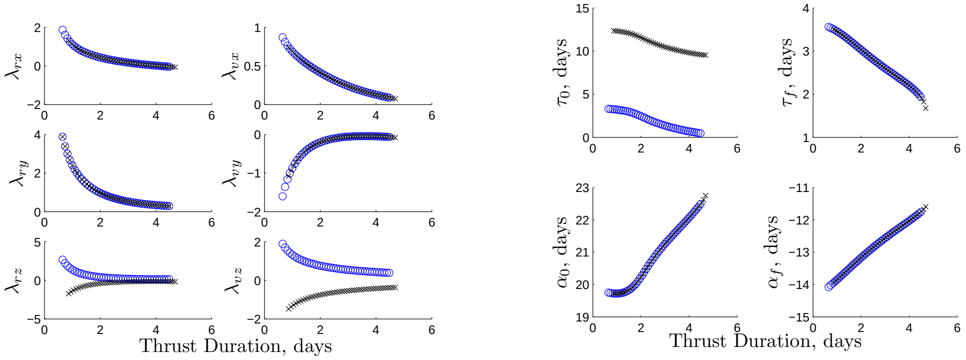

Initial co-states     Timelike parameters

**Figure 12. Initial values of $L_1$ vertical to $L_2$ northern (black) and southern (blue) halo transfers.**

location along the thrust arc where the $I_{sp}$ constraints are already satisfied. The state vector then becomes

$$\boldsymbol{X} = \left\{\begin{matrix} \tau_0 \\ \alpha_0 \\ \boldsymbol{\lambda}_1 \\ \kappa_1 \\ \boldsymbol{\xi}_2 \\ \kappa_2 \\ \vdots \\ \boldsymbol{\xi}_n \\ \kappa_n \\ \kappa_T \\ \alpha_f \\ \tau_f \end{matrix}\right\} \tag{45}$$

The elements of the constraint gradient are then represented as

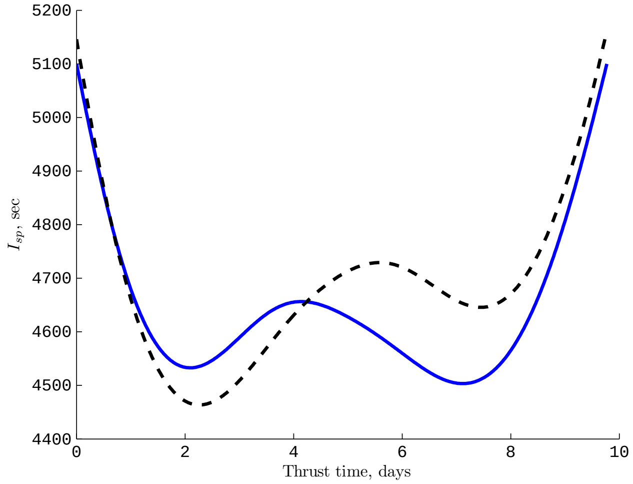

**Figure 13. Time history of $I_{sp}$ for unconstrained (dashed) and constrained (blue) trajectory.**

$$DF(\boldsymbol{X}) = \begin{bmatrix} \mathbf{0} & \mathbf{0} & \frac{\partial I_{sp}}{\partial \boldsymbol{\lambda}_v} & \pm 2\kappa_1 & \mathbf{0} & \cdots & & & & \mathbf{0} \\ \boldsymbol{\Psi}_{1,\boldsymbol{rv}} \frac{\partial \boldsymbol{x}_I}{\partial \tau_0} & \boldsymbol{\Psi}_{1,\boldsymbol{rv}} \frac{\partial \boldsymbol{x}_I}{\partial \alpha_0} & \boldsymbol{\Psi}_{1,\boldsymbol{\lambda}} & \mathbf{0} & -\mathbf{I}_{14} & \mathbf{0} & \cdots & & & \mathbf{0} \\ \mathbf{0} & \mathbf{0} & \mathbf{0} & \mathbf{0} & \frac{\partial I_{sp}}{\partial (m,\boldsymbol{\lambda})} & \pm 2\kappa_2 & \mathbf{0} & \cdots & & \mathbf{0} \\ \mathbf{0} & \mathbf{0} & \mathbf{0} & \mathbf{0} & \Psi_2 & \mathbf{0} & -\mathbf{I}_{14} & \mathbf{0} & \cdots & \mathbf{0} \\ \vdots & & & & & & & \ddots & & \mathbf{0} \\ \mathbf{0} & \cdots & & \cdots & \mathbf{0} & -\mathbf{I}_{14} & \mathbf{0} & \mathbf{0} & \mathbf{0} & \mathbf{0} \\ \mathbf{0} & \cdots & & \cdots & \mathbf{0} & \frac{\partial I_{sp}}{\partial (m,\boldsymbol{\lambda})} & \pm 2\kappa_n & \mathbf{0} & \mathbf{0} & \mathbf{0} \\ \mathbf{0} & \cdots & & \cdots & \mathbf{0} & \Psi_{\boldsymbol{rv},n} & \mathbf{0} & \mathbf{0} & -\frac{\partial \boldsymbol{x}_T}{\partial \alpha_f} & -\frac{\partial \boldsymbol{x}_T}{\partial \tau_f} \\ \mathbf{0} & \cdots & & \cdots & \mathbf{0} & \frac{\partial I_{sp}}{\partial (m,\boldsymbol{\lambda})} \boldsymbol{\Psi}_{n,m\boldsymbol{\lambda}} & \mathbf{0} & \pm 2\kappa_T & \mathbf{0} & \mathbf{0} \end{bmatrix} \tag{46}$$

Note that this gradient is also sparse and that no numerical derivatives are required.

The specific trajectory to be constrained is the 9.77-day transfer from the first sample mission application, that is, a transfer from one $L_1$ halo orbit to another. The upper limit on $I_{sp}$ is specified as 5100s and the lower limit is 4500s, and the thrust arc segments are defined so that the patch points are located at times corresponding to the local extrema in $I_{sp}$. Applying the constraint on $I_{sp}$ only slightly shifts the physical path of the spacecraft and, indeed, the final mass is nearly equal, that is, the unconstrained value is 498.40 kg and the constrained result equals 498.37 kg. Yet, the behavior of the $I_{sp}$ for the transfer is noticeably modified as demonstrated in Fig. 13. While the constrained trajectory fits within the limits on $I_{sp}$, it is interesting to note that the global minimum has switched locations.

## VI. Summary and Recommendations

A method for constructing fuel optimal transfers between libration point orbits using a variable specific impulse engine and invariant manifolds has been developed and applied to several different scenarios. The low dimensionality of indirect optimization has been combined with the flexibility of direct optimization to produce a hybrid algorithm that allows for the addition of constraints on the trajectory. Though the general method can be applied to any system, the examples in this investigation are based in the Earth-moon restricted problem and showcase transfers with and without constraints or incorporation of the invariant manifolds. The major results of this work are:

- Transfer families between two $L_1$ halo orbits are computed and the $I_{sp}$ behavior for varying thrust durations is investigated.

- $L_1$ northern halo to $L_2$ northern and southern halo transfers are studied, where transfers between opposing orbits (that is north-to-south) follow natural system dynamics and are, thus, more fuel efficient with a shorter total transfer time.
- System symmetry yields transfers from an $L_1$ vertical orbit to an $L_2$ northern halo to mirror transfers to a southern halo, and this symmetry potentially applies to other transfers, offering a useful tool for mission design in low-thrust scenarios.
- An example that includes a constraint on $I_{sp}$ demonstrates the blending of multiple shooting and direct optimization techniques to satisfy specific mission goals or address spacecraft limitations.

Some suggestions for future work are:

- Incorporating more realistic models for Earth and moon motion, along with perturbation effects from the Sun and non-spherical gravitational models. Of particular interest are the symmetry effects noted for the CR3BP and their translation to the higher fidelity models.
- Constructing transfers between a wider variety of orbits and with different combinations of invariant manifolds.
- Applying other path constraints to the transfers, such as shadowing or line-of-sight requirements.
- Incorporating global optimization techniques to study the full trade space of transfers.

Ultimately, the methods presented combine the rapid calculation of low-dimensioned indirect optimization with the flexibility of higher-dimensioned direct optimization. In addition, several characteristics of a variable specific impulse engine operating in a multibody regime are investigated, providing an aid in future mission design.

## VII. Acknowledgments

This work was conducted at Purdue University; the second author was supported by the NASA Graduate Student Researchers Program (GSRP) fellowship under NASA Grant number NNX07A017H. Many thanks to Wayne Schlei, who helped immensely with the orbit and manifold images.

## Appendix

The $14 \times 14$ expansion for $\mathbf{A}(t)$ is:

$$\mathbf{A}(t) = \begin{bmatrix} 0_3 & \mathbf{I}_3 & 0_{3,1} & 0_3 & 0_{3,1} & 0_{3,1} & 0_{3,1} & 0_{3,1} \\ & & -\frac{2P_{\max}\lambda_{\boldsymbol{v}_x}}{m^3\lambda_m} & 0_{1,3} & \frac{P_{\max}}{m^2\lambda_m} & 0 & 0 & -\frac{P_{\max}\lambda_{\boldsymbol{v}_x}}{m^2\lambda_m^2} \\ \frac{\partial \boldsymbol{f}_1}{\partial \boldsymbol{r}} & \frac{\partial \boldsymbol{f}_1}{\partial \boldsymbol{v}} & -\frac{2P_{\max}\boldsymbol{\lambda}_{\boldsymbol{v}_y}}{m^3\lambda_m} & 0_{1,3} & 0 & \frac{P_{\max}}{m^2\lambda_m} & 0 & -\frac{P_{\max}\lambda_{\boldsymbol{v}_y}}{m^2\lambda_m^2} \\ & & -\frac{2P_{\max}\lambda_{\boldsymbol{v}_z}}{m^3\lambda_m} & 0_{1,3} & 0 & 0 & \frac{P_{\max}}{m^2\lambda_m} & -\frac{P_{\max}\lambda_{\boldsymbol{v}_x}}{m^2\lambda_m^2} \\ 0_{1,3} & 0_{1,3} & \frac{P_{\max}\lambda_{\boldsymbol{v}}^2}{m^3\lambda_m^2} & 0_{1,3} & -\frac{P_{\max}\lambda_{\boldsymbol{v}_x}}{m^2\lambda_m^2} & -\frac{P_{\max}\lambda_{\boldsymbol{v}_y}}{m^2\lambda_m^2} & -\frac{P_{\max}\lambda_{\boldsymbol{v}_z}}{m^2\lambda_m^2} & \frac{P_{\max}\lambda_{\boldsymbol{v}}^2}{m^2\lambda_m^3} \\ -\mathbf{W} & 0_3 & 0_{3,1} & 0_3 & & -\left(\frac{\partial \boldsymbol{f}_1}{\partial \boldsymbol{r}}\right)^T & & 0_{3,1} \\ 0_3 & 0_3 & 0_{3,1} & -\mathrm{I}_3 & & -\left(\frac{\partial \boldsymbol{f}_1}{\partial \boldsymbol{v}}\right)^T & & 0_{3,1} \\ 0_{1,3} & 0_{1,3} & -\frac{3P_{\max}\lambda_{\boldsymbol{v}}^2}{m^4\lambda_m} & 0_{1,3} & \frac{2P_{\max}\lambda_{\boldsymbol{v}_x}}{m^2\lambda_m} & \frac{2P_{\max}\lambda_{\boldsymbol{v}_y}}{m^2\lambda_m} & \frac{2P_{\max}\lambda_{\boldsymbol{v}_z}}{m^2\lambda_m} & -\frac{P_{\max}\lambda_{\boldsymbol{v}}^2}{m^3\lambda_m^2} \end{bmatrix}$$

where the subscripts on $\mathbf{0}$ and $\mathbf{I}$ indicate the size of the zero or identity matrix (‘3’ indicates a $3 \times 3$ matrix, ‘3,1’ a 3-element column vector, and ‘1,3’ a 3-element row vector), and where

$$\mathbf{W} = \begin{bmatrix} (\lambda_{\boldsymbol{v}_x}U_{x^3} + \lambda_{\boldsymbol{v}_y}U_{x^2y} + \lambda_{\boldsymbol{v}_z}U_{x^2z}) & (\lambda_{\boldsymbol{v}_x}U_{x^2y} + \lambda_{\boldsymbol{v}_y}U_{xy^2} + \lambda_{\boldsymbol{v}_z}U_{xyz}) & (\lambda_{\boldsymbol{v}_x}U_{x^2z} + \lambda_{\boldsymbol{v}_y}U_{xyz} + \lambda_{\boldsymbol{v}_z}U_{xz^2}) \\ (\lambda_{\boldsymbol{v}_x}U_{x^2y} + \lambda_{\boldsymbol{v}_y}U_{xy^2} + \lambda_{\boldsymbol{v}_z}U_{xyz}) & (\lambda_{\boldsymbol{v}_x}U_{xy^2} + \lambda_{\boldsymbol{v}_y}U_{y^3} + \lambda_{\boldsymbol{v}_z}U_{y^2z}) & (\lambda_{\boldsymbol{v}_x}U_{xyz} + \lambda_{\boldsymbol{v}_y}U_{y^2z} + \lambda_{\boldsymbol{v}_z}U_{yz^2}) \\ (\lambda_{\boldsymbol{v}_x}U_{x^2z} + \lambda_{\boldsymbol{v}_y}U_{xyz} + \lambda_{\boldsymbol{v}_z}U_{xz^2}) & (\lambda_{\boldsymbol{v}_x}U_{xyz} + \lambda_{\boldsymbol{v}_y}U_{y^2z} + \lambda_{\boldsymbol{v}_z}U_{yz^2}) & (\lambda_{\boldsymbol{v}_x}U_{xz^2} + \lambda_{\boldsymbol{v}_y}U_{yz^2} + \lambda_{\boldsymbol{v}_z}U_{z^3}) \end{bmatrix}$$

Note that the matrix $\mathbf{W}$ is symmetric and incorporates third partials of the pseudo-potential function $U$:

$$U = \frac{1-\mu}{d_1} + \frac{\mu}{d_2} + \frac{1}{2}(x^2 + y^2)$$

This completes the expansion for $\mathbf{A}(t)$.

# References

[1] Goebel, D., Brophy, J., Polk, J., Katz, I., and Anderson, J., "Variable Specific Impulse High Power Ion Thruster." Paper No. AIAA 2005-4246, *AIAA/ASME/SAE/ASEE Joint Propulsion Conference & Exhibit*, Tucson, Arizona, July 10-13, 2005.

[2] "VASIMR Technology," Ad Astra Rocket Company, `http://www.adastrarocket.com/aarc/Technology`, 2010 [accessed March 20, 2010].

[3] Komurasaki, K., Arakawa, Y., and Takegahara, H., "An Overview of Electric and Advanced Propulsion Activities in Japan." *Proceedings of the Third International Conference of Spacecraft Propulsion*, Cannes, France, October 10-13, 2000. Cannes, France, pp. 27-39.

[4] Volle, M., "Optimal Variable-Specific-Impulse Rendezvous Trajectories Between Halo Orbits,", Paper No. ISTS 2006-d-73, *International Symposium on Space Flight Dynamics*, Kanazawa, Japan, June 4-11, 2006.

[5] Russell, R., "Primer Vector Theory Applied to Global Low-Thrust Trade Studies." *Journal of Guidance, Control, and Dynamics*, Vol. 30, No. 2, March-April 2007, pp. 460-473.
doi:10.2514/1.22984

[6] Senent, J., Ocampo, C., and Capella, A., "Low-Thrust Variable-Specific-Impulse Transfers and Guidance to Unstable Periodic Orbits." *Journal of Guidance, Control, and Dynamics*, Vol. 28, No. 2, March-April 2005, pp. 280-290.
doi:10.2514/1.6398

[7] Mingotti, G, Topputo, F., and Bernelli-Zazzera, F., "Combined Optimal Low-Thrust and Stable-Manifold Trajectories to the Earth-Moon Halo Orbits." *New Trends in Astrodynamics and Applications III*, Vol. 886, February 2007, pp. 100-112.
doi:10.1063/1.2710047

[8] Martin, C., and Conway, B., "Optimal Low-Thrust/Invariant Manifold Earth Moon Transfer Trajectories." Paper No. AAS 10-105, *AAS/AIAA Space Flight Mechanics Meeting*, San Diego, California, February 14-17, 2010.

[9] Betts, J., "Survey of Numerical Methods for Trajectory Optimization." *Journal of Guidance, Control, and Dynamics*, Vol. 21, No. 2, March-April 1998, pp. 193-207.
doi:10.2514/2.4231

[10] Kluever, C., and Pierson, B., "Optimal Low-Thrust Three-Dimensional Earth-Moon Trajectories." *Journal of Guidance, Control, and Dynamics*, Vol. 18, No. 4, July-August 1995, pp. 830-837.

[11] Ozimek, M., and Howell, K., "Low-Thrust Transfers in the Earth-Moon System Including Applications to Libration Point Orbits." *Journal of Guidance, Control, and Dynamics*, Vol. 33, No. 2, March-April, 2010, pp. 533-549.

[12] D. Lawden, *Optimal Trajectories for Space Navigation.* Butterworths, London, 1963, pp. 54-126.

[13] Gill, P., Murray, W., and Saunders, M., "SNOPT: An SQP Algorithm for Large-Scale Constrained Optimization." *SIAM Review*, Vol. 47, No. 1, 2005, pp. 99-131.